

# Fast tomoelastography of the mouse brain by multifrequency single-shot MR elastography

Gergely Bertalan<sup>1</sup> | Jing Guo<sup>1</sup> | Heiko Tzschätzsch<sup>1</sup> | Charlotte Klein<sup>2</sup> |  
Eric Barnhill<sup>1</sup>  | Ingolf Sack<sup>1</sup> | Jürgen Braun<sup>3</sup> 

<sup>1</sup>Department of Radiology, Charité–Universitätsmedizin Berlin, Campus Charité Mitte, Berlin, Germany

<sup>2</sup>Department of Neurology, Charité–Universitätsmedizin Berlin, Campus Charité Mitte, Berlin, Germany

<sup>3</sup>Institute of Medical Informatics, Charité–Universitätsmedizin Berlin, Campus Benjamin Franklin, Berlin, Germany

## Correspondence

Jürgen Braun, Institute of Medical Informatics, Charité–Universitätsmedizin Berlin, Hindenburgdamm 30, 12200 Berlin, Germany.  
Email: juergen.braun@charite.de

## Funding information

Deutsche Forschungsgemeinschaft, Grant/Award Number: GRK 2260

**Purpose:** To introduce in vivo multifrequency single-shot magnetic resonance elastography for full-FOV stiffness mapping of the mouse brain and to compare in vivo stiffness of neural tissues with different white-to-gray matter ratios.

**Methods:** Viscous phantoms and 10 C57BL-6 mice were investigated by 7T small-animal MRI using a single-shot spin-echo planar imaging magnetic resonance elastography sequence with motion-encoding gradients positioned before the refocusing pulse. Wave images were acquired over 10 minutes for 6 mechanical vibration frequencies between 900 and 1400 Hz. Stiffness maps of shear wave speed (SWS) were computed using tomoelastography data processing and compared with algebraic Helmholtz inversion (AHI) for signal-to-noise ratio (SNR) analysis. Different brain regions were analyzed including cerebral cortex, corpus callosum, hippocampus, and diencephalon.

**Results:** In phantoms, algebraic Helmholtz inversion–based SWS was systematically biased by noise and discretization, whereas tomoelastography-derived SWS was consistent over the full SNR range analyzed. Mean in vivo SWS of the whole brain was  $3.76 \pm 0.33$  m/s with significant regional variation (hippocampus =  $4.91 \pm 0.49$  m/s, diencephalon =  $4.78 \pm 0.78$  m/s, cerebral cortex =  $3.53 \pm 0.29$  m/s, and corpus callosum =  $2.89 \pm 0.17$  m/s).

**Conclusion:** Tomoelastography retrieves mouse brain stiffness within shorter scan times and with greater detail resolution than classical algebraic Helmholtz inversion–based magnetic resonance elastography. The range of SWS values obtained here indicates that mouse white matter is softer than gray matter at the frequencies investigated.

## KEYWORDS

elasticity, mouse brain, multifrequency magnetic resonance elastography, shear wave speed

## 1 | INTRODUCTION

Brain mechanical properties influence many vital neurological functions including brain development, metabolism, and

tissue repair.<sup>1</sup> However, studying brain mechanical properties in a noninvasive fashion encounters a number of challenges including the fact that the brain is protected by the skull as well as the heterogeneous and complex geometry

of the brain.<sup>2</sup> At present, magnetic resonance elastography (MRE) is the sole modality allowing noninvasive measurement of in vivo brain mechanical properties in patients and small animals.<sup>3,4</sup>

Whereas in patients MRE has been demonstrated to provide maps of elasticity and viscosity (elastograms) with high detail resolution,<sup>5,6</sup> the quality of MRE elastograms of mouse brain is more limited. Reasons for this include the lack of time-efficient MRE sequences for preclinical MRI systems as well as challenges regarding the transmission of high-frequency mechanical vibrations into the relatively small mouse brain. Overall, state-of-the-art cerebral MRE techniques in the mouse still lag behind methods optimized for human brain MRE.<sup>2</sup> For example, cerebral MRE in a clinical setting requires scan times of approximately 10 minutes for acquisition with 8 dynamics and 7 stimulation frequencies<sup>7</sup> or full brain coverage at single frequency.<sup>8</sup> In contrast, MRE of the mouse brain takes more than 15 minutes for single-component acquisition at single drive frequency (Table 1).<sup>9-12</sup> Consequently, solutions to the inverse problem in MRE for recovery of the shear modulus, which rely on multiple acquisitions, require very long scan times or cannot be applied to the murine brain.

Inverse problem solutions in MRE incorporate formulations of the wave equation based on finite differences or finite elements.<sup>13-16</sup> Alternatively, phase gradient methods are used, which incorporate directional filters to decompose the wave field into single-directional (plane-wave) components whose spatial derivatives are scaled by wave numbers.<sup>17</sup> The

wave numbers retrieved from multifrequency wave fields can be combined and inverted to compute compound maps of wave speed.<sup>18</sup> This strategy, introduced in the literature as “tomoelastography,” has been demonstrated to be a noise-robust method for full-FOV MRE in abdominal and pelvic organs, providing high detail resolution and consistent values with respect to physiological and pathological alterations of mechanical tissue properties in vivo.<sup>19-21</sup>

However, tomoelastography of the human brain is degraded by an abundance of solid-fluid (slip) interfaces that disturb directional filters because of marked changes of local wavenumbers.<sup>2</sup> The murine cortex differs from the human cortex in that it is less folded and has fewer sulci, potentially reducing artifacts related to slip boundaries. This would favor tomoelastography for investigation of the mouse brain, where it is expected to provide sharper details and more consistent values than conventional MRE. If feasible in the mouse brain, tomoelastography could be useful for the preclinical investigation of a wide range of pathological and localized alterations including Alzheimer’s disease,<sup>11,22</sup> Parkinson’s disease,<sup>10,23</sup> multiple sclerosis,<sup>12,24</sup> demyelination,<sup>25</sup> stroke,<sup>26</sup> hydrocephalus,<sup>27</sup> tumors,<sup>28</sup> and functional activation.<sup>29</sup> Moreover, basic research into the relationship between tissue structures and macroscopic mechanical properties of the brain could be conducted in mouse tissue rather than in human brain.<sup>1,30</sup>

Because tomoelastography relies on multifrequency wave inversion, we will first introduce fast MRE data acquisition suitable for small-animal MRI, to capture wave fields at different frequencies within short times. The feasibility

**TABLE 1** Stiffness estimates of the mouse brain measured by in vivo MRE and reported in the literature

	Vibration frequency (Hz)	SWS (m/s) (mean ± SD)	Resolution (mm) (ip × ip × slt)	Normalized scan time (min) <sup>a</sup>	Dimension of data analysis
Atay et al <sup>9</sup>	1200	3.93 ± 0.45	0.25 × 0.25 × 0.40	8	3D
Clayton et al <sup>55</sup>	600-1800	1.42 ± 2.97 <sup>b</sup>	0.25 × 0.25 × 0.25	22 <sup>c</sup>	3D
Jamin et al <sup>56</sup>	1000	2.85 ± 0.04	0.15 × 0.15 × 0.30	8	3D
Boulet et al <sup>57</sup>	877.5	3.04 ± 0.04	0.16 × 0.16 × 1.00	60	2D
Hain et al <sup>23</sup>	900	2.35 ± 0.05 <sup>d</sup>	0.20 × 0.20 × 2.00	20 <sup>c</sup>	2D
Klein et al <sup>10</sup>	900	2.35 ± 0.12	0.20 × 0.20 × 2.00	20 <sup>c</sup>	2D
Riek et al <sup>12</sup>	900	2.56 ± 0.03	0.20 × 0.20 × 2.00	20 <sup>c</sup>	2D
Millward et al <sup>24</sup>	900	2.46 ± 0.13	0.20 × 0.20 × 2.00	12 <sup>c</sup>	2D
Schregel et al <sup>25</sup>	1000	2.86 ± 0.18 <sup>e</sup>	0.15 × 0.15 × 0.30	n.a.	3D
Munder et al <sup>22</sup>	900	2.65 ± 0.10	0.25 × 0.25 × 1.00	20 <sup>c</sup>	2D
Present study AHI	900-1400	2.69 ± 0.14	0.18 × 0.18 × 1.00	0.6	2D
Present study tomoelastography	900-1400	3.76 ± 0.33	0.18 × 0.18 × 1.00	0.6	2D

Note: The values (mean ± SD) have been translated to SWS based on Eq. 1. Resolution is given for the imaging plane and slice thickness.

Abbreviations: ip, imaging plane; n.a., not available; slt, slice thickness.

<sup>a</sup>Given scan times are normalized to the acquisition of 1 wave field component and 1 average.

<sup>b</sup>No SD available.

<sup>c</sup>Phase difference method.

<sup>d</sup>Average values of the data for midbrain, hippocampus, and substantia nigra.

<sup>e</sup>Average values of the data for corpus callosum.

of single-shot multifrequency MRE in a preclinical setting based on asymmetric motion encoding combined with tomoelastography data processing will be demonstrated in a phantom and compared with compact 0.5T MRE. In a second step, we will apply the new method to *in vivo* mouse brain to investigate details of stiffness variation among different brain regions. For consistency we will use the term “stiffness” only for discussion of relative differences in shear wave speed (SWS), the actually measured quantity in tomoelastography, and use SWS otherwise.<sup>31</sup>

The overall aim of this paper is 3-fold: (1) introduce a methodology for fast high-resolution brain elastography in the mouse based on single-shot wave image acquisitions; (2) analyze SNR performance of the new sequence as well as discretization artifacts encountered by tomoelastography data processing; and (3) investigate stiffness ratios between neural tissues with different proportions of white and gray matter. To this end, we will tabulate the reference SWS values for several subregions of the mouse brain including the cortex, hippocampus, and corpus callosum.

## 2 | METHODS

### 2.1 | Phantoms

Two cylindrical phantoms made of ultrasound gel (Sonogel, Germany) were investigated at room temperature. One

sample with a diameter of 13.3 mm was investigated in a 7T small-animal MRI scanner (Bruker BioSpec 70/16, Ettlingen, Germany) using the newly developed imaging method described subsequently. A second sample with 7.5-mm diameter was investigated in a compact 0.5T tabletop MRE device (Pure Devices, Würzburg, Germany), which we used as a reference standard.<sup>32</sup>

### 2.2 | Animals

The study was approved by our local animal ethics committee (Landesamt für Gesundheit und Soziales, Berlin, Germany) and was executed in accordance with the European Community’s Council Directive of November 24, 1986 (86/609/EEC). Ten healthy 6-week-old female C57BL-6 mice were used for *in vivo* measurements. The animals were anesthetized with 1.5% isoflurane during the experiments. Body temperature was kept constant by circulating water warming pads (41°C) integrated into a custom-built animal holder (Figure 1A).

### 2.3 | Magnetic resonance elastography

Experiments were performed on a 7T preclinical MRI scanner running ParaVision 6.1 software and using a 20-mm-diameter 1H-RF quadrature volume coil (RAPID Biomedical, Würzburg, Germany). A custom-made driver

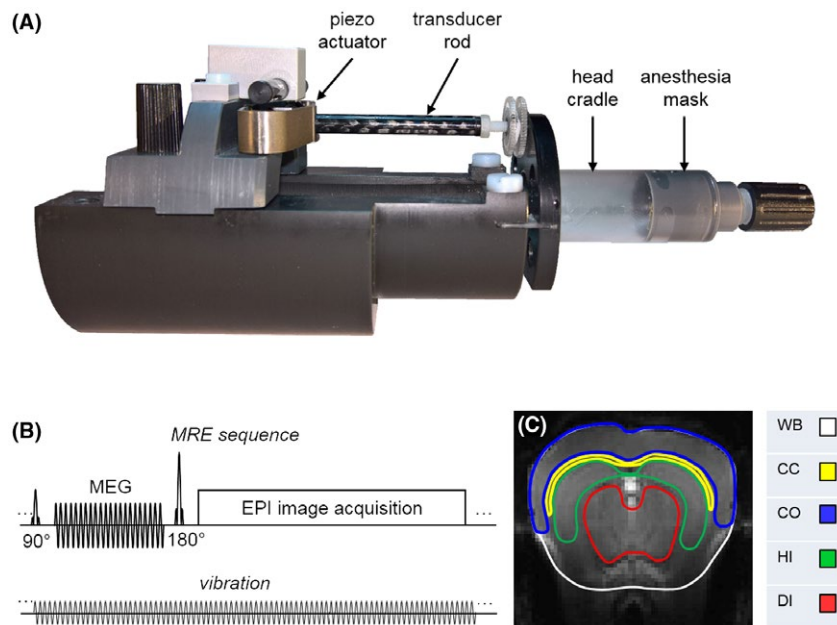


**FIGURE 1** Setup of magnetic resonance elastography (MRE) of the mouse brain. A, Main components of the transducer system including piezo actuator, transducer rod, and head cradle with integrated anesthesia mask. B, Single-shot spin-echo EPI-MRE pulse sequence. The motion-encoding gradients (MEGs) are deployed before the refocusing pulse (asymmetrically with respect to the 180° pulse), and the number of MEG cycles is adapted to fit into  $TE/2$ . The 22 MEG cycles shown correspond to a vibration frequency of 900 Hz. C, Regions of interest analyzed in the present study. Abbreviations: CC, corpus callosum; CO, cerebral cortex; DI, diencephalon; HI, hippocampus; WB, whole brain

system was developed for introducing mechanical waves into the brain (Figure 1A). Mechanical oscillations with frequencies of 900, 1000, 1100, 1200, 1300, and 1400 Hz and approximately 60- $\mu\text{m}$  peak-to-peak displacement amplitude perpendicular to the principal axis of the magnetic field were generated by a nonmagnetic piezoceramic actuator (CEDRAT Technologies, Meylan Cedex, France). The actuator was supplied by a low-current transistor–transistor logic function generator (CGC Instruments, Chemnitz, Germany). The function generator was synchronized to the scanner clock based on a 10-MHz pulsed signal (to avoid any latency of the wave relative to the scanner after minutes of continuous vibrations) and controlled by “smart triggers” (to initiate the vibration and to allow automatic selection of vibration frequency, number of cycles, and signal amplitudes by the imaging protocol).<sup>19</sup> The vibrations were transferred into the head cradle of the animal holder through a carbon fiber rod.

Displacement fields were acquired in 5 axial slices through the mouse brain using a modified spin-echo EPI sequence with sinusoidal motion-encoding gradients, which are deployed before the refocusing pulse (Figure 1B). The number of motion-encoding gradient cycles was adapted to the motion-encoding gradient frequency (which was identical to the vibration frequency), to fit into a fixed time frame of 25 ms, yielding 22 cycles (900 Hz), 25 cycles (1000 Hz), 27 cycles (1100 Hz), 30 cycles (1200 Hz), 32 cycles (1300 Hz), and 35 cycles (1400 Hz). To capture the full field of motion, polarization of the motion-encoding gradients (amplitude of 482 mT/m) was switched in consecutive experiments along all 3 Cartesian directions of the imaging coordinate system. Eight time points, equally spaced over a full oscillation period, were acquired to assess the dynamics of the wave field.

Further acquisition parameters were TR = 1500 ms, TE = 67 ms, matrix size = 90  $\times$  80, EPI readout duration = 36 ms, FOV = 16.2  $\times$  14.4 mm<sup>2</sup>, in-plane resolution = 0.18 mm  $\times$  0.18 mm, slice thickness = 1 mm, and 2 signal averages to increase the SNR. The total scan time per animal (5 slices, 6 vibration frequencies, 8 wave dynamics, 3 field components, and 2 averages) was approximately 8 minutes. Additionally, different spatial resolutions were tested with matrix sizes of 100  $\times$  110 (0.14  $\times$  0.14 mm), 90  $\times$  110 (0.16  $\times$  0.16 mm), and 80  $\times$  80 (0.2  $\times$  0.2 mm), yielding readout times of 55, 45 and 32 ms, respectively, whereas TE was kept constant with 67 ms.

Setup and imaging parameters for phantom experiments at 7T were similar using a cylindrical sample container (inner diameter = 13.3 mm; length = 20 mm), which was inserted into the head cradle. This setup allowed us to induce well-defined cylindrical waves for Bessel fit–based SWS analysis.<sup>32–34</sup> Vibration frequencies were 800 Hz to 1200 Hz (100-Hz increments)—the same as the vibration frequency range used in 0.5T tabletop MRE for reference.<sup>32,35</sup>

## 2.4 | Shear wave speed recovery and data analysis

The following 3 SWS reconstruction methods were used:

1. Fitting of cylindrical waves in phantoms based on Bessel functions.<sup>32–34</sup> This method was applied to 7T and 0.5T data and was considered the reference standard. Furthermore, a fit of the spatially averaged SWS over frequency (dispersion function) was performed based on the springpot model, yielding 2 model parameters: the shear modulus  $\mu$  and the dimensionless power-law exponent  $\alpha$ .<sup>2</sup>
2. Algebraic Helmholtz inversion (AHI) based on 5-tap Laplacian operator kernels. After AHI, complex shear modulus  $G^* = G' + i^*G''$  was converted to SWS using the following equation:

$$\text{SWS}(\omega) = \frac{1}{\text{Re}\left(\sqrt{\frac{\rho}{G(\omega)}}\right)} = \sqrt{\frac{2(G' + G'')^2}{\rho(G' + \sqrt{G'^2 + G''^2})}} \quad (1)$$

where  $\omega$  is the angular drive frequency.

3. Tomoelastography as detailed in Ref. 18. Briefly, wave numbers were reconstructed from plane waves obtained by applying 8 directional filters for each single-frequency, single-component wave image. Before inversion to SWS, wave numbers ( $k$ ) were amplitude-weighted and averaged over all directions, components, and frequencies to compensate for wave voids occurring in single images. As introduced in Ref. 18, we will use  $k$ -MDEV (multifrequency dual elastoviscous) inversion to refer to tomoelastography data processing.

Regional SWS values were derived from regions of interest manually drawn on the central slice of the MRE magnitude data set for anatomical compliance. The selected regions of interest consisted of the anatomical regions of overall brain parenchyma (whole brain [WB], cerebral cortex [CO], corpus callosum [CC], hippocampus [HI], and the diencephalon [DI], consisting primarily of the thalamus and hypothalamus) (Figure 1C).

## 2.5 | Signal-to-noise ratio measurements and analysis of discretization biases

We propose using the blind noise estimation method of Donoho et al.,<sup>36</sup> arguably the most common blind noise estimation method in current practice. As this method estimates the noise from the statistical distribution of the image, it is

simple to constrain the estimate to the anatomical regions of the acquisition using a binary mask. Furthermore, this method estimates noise in the wavelet domain, which would be expected to be very well suited to MRE wave images, as a wavelet basis is optimally sparse for wave images with discontinuities.<sup>37,38</sup>

For a wavelet decomposition of an image into  $1..N$  logarithmic scales using wavelet filter  $\phi$  and scaling filter  $\psi$ , the image noise in Ref. 36 is estimated as  $\sigma_n = \text{MAD}(\phi_N/0.6745)$ , which is the median absolute deviation (MAD) of the finest band of wavelet coefficients, scaled by a normalizing constant, as explained in Ref. 36. To generate an SNR measurement,  $\frac{\sigma_s}{\sigma_n}$  is used, in which  $\sigma_s$  is the estimated signal power. As the MRE acquisition has 3 channels (the encoding directions  $x$ ,  $y$ , and  $z$ ), we can use a vectorial SNR estimate that disregards covariances and therefore reduces to the ratio of the sums. Therefore, our final formula is

$$\text{SNR} = \frac{\sum_{x,y,z} \sigma_s}{\sum_{x,y,z} \sigma_n} \quad (2)$$

Recent work<sup>39,40</sup> has suggested using the SNR of the images of numerically estimated derivatives as a determinant of image quality, rather than the images of the displacements, as the numerical derivatives have an outsize effect on the wave inversion. Here we follow this approach, producing vectorial SNR measurements of the displacement image and the Laplacian images (which contain only second derivatives), and a scalar SNR estimate for the octahedral shear strain image (i.e., a single image generated from combining first derivatives). Henceforth, we use 3 SNR measures: (1) displacement SNR (either calculated from single or multiple field components), (2) strain SNR (octahedral shear strain, which requires all 3 wave field components), and (3) Laplacian SNR. The 3 SNR-computation methods can be found online and used for any MRI data (bioqic-apps.charite.de). Discretization biases are analyzed by SWS as a function of spatial support ( $N$ , number of pixels per wavelength) and SNR. Both variables affect the outcome of the inversion-based SWS values in MRE.

## 2.6 | Statistical analysis

Stiffness difference among the anatomical regions was tested using the Wilcoxon rank sum test with the built-in function rank sum of MATLAB (MathWorks, Natick, MA). For  $P$  values less than 0.05, differences were considered as significant.

## 3 | RESULTS

### 3.1 | Simulations and phantom experiments

The top line of Figure 2 shows the cylindrical wave images that were simulated using a Bessel function of the first

kind,<sup>32</sup> based on the parameters measured and recovered in the phantom as shown in the second and third line (real parts of complex-valued deflections). The frequency-resolved wave images were acquired by new single-shot EPI MRE at 7T and (for reference) by 0.5T tabletop MRE. The mean SNR of EPI-MRE wave images was  $23.8 \pm 5.7$  (displacement) and  $2.6 \pm 0.9$  (Laplacian). Figure 3A shows springpot fitting curves and spatially averaged SWS values obtained using Bessel fit, AHI, and tomoelastography ( $k$ -MDEV). The SWS values resulting from Bessel regression and the fitting curve of the springpot model (7T: squares and solid line versus 0.5T: circles and dashed line) are in very good agreement for the 2 MRI scanners (7T:  $\alpha = 0.17$  and  $\mu = 600$  Pa versus 0.5T:  $\alpha = 0.18$  and  $\mu = 590$  Pa). Taking Bessel fit values as reference (median SWS = 0.97 m/s),  $k$ -MDEV slightly overestimates SWS (4.1%, median SWS = 1.01 m/s), whereas AHI yields a 3-fold greater overestimation (12.9%, median SWS = 1.12 m/s). The AHI overshoot is well reproduced by numerical data shown in Figure 3B. Figure 3B demonstrates by simulated waves with added Gaussian noise (displacement SNR from 1.1 to 46) that AHI imposes greater inversion bias than  $k$ -MDEV. Simulated waves from 800 Hz to 1200 Hz shown in the top line of Figure 2 were used for the soft-material inversion (mean SWS = 0.97 m/s), whereas for the stiff material a SWS of 3.45 m/s was assumed, which agrees with the in vivo experiments. Spatial support  $N$  (pixels per wavelength, as denoted in Eq. 1 of Arunachalam et al.<sup>41</sup>) was 8.1 in the soft material, whereas  $N$  was between 17 and 25 for in vivo data. Because  $N$  and SNR have adverse effects on the apparent SWS,<sup>16,41</sup> the ratio  $N/\text{SNR}$  is plotted on the  $x$ -axis. Dependent on the ratio  $N/\text{SNR}$ , the dispersion-by-inversion bias can cause either an overshoot or undershoot of values, both enhanced by second-order finite derivative methods such as AHI. At  $N/\text{SNR} \approx 0.2$ , which is the frequency-averaged value for 7T MRE in the relatively soft phantom, Figure 3B reveals an overestimation of SWS by AHI in the order of 10%. The value of  $k$ -MDEV, based on single-order gradients, is less susceptible to the dispersion-by-inversion bias, yielding deviations of 2% within the entire range of  $N/\text{SNR}$  of Figure 3B. Note that the larger overestimation of  $k$ -MDEV in Figure 3A compared with Figure 3B is a result of single-frequency (A) versus multi-frequency analysis (B).

### 3.2 | In vivo MRE

Representative frequency-resolved complex-valued wave images (real parts) obtained in 1 mouse are shown in Figure 4A. The mean SNR values accounting for displacement, strain, and Laplacian were  $7.7 \pm 2.4$ ,  $2.24 \pm 0.5$ , and  $0.8 \pm 0.06$ , respectively. Figure 4B,C show frequency-resolved AHI and  $k$ -MDEV-SWS maps, respectively. The

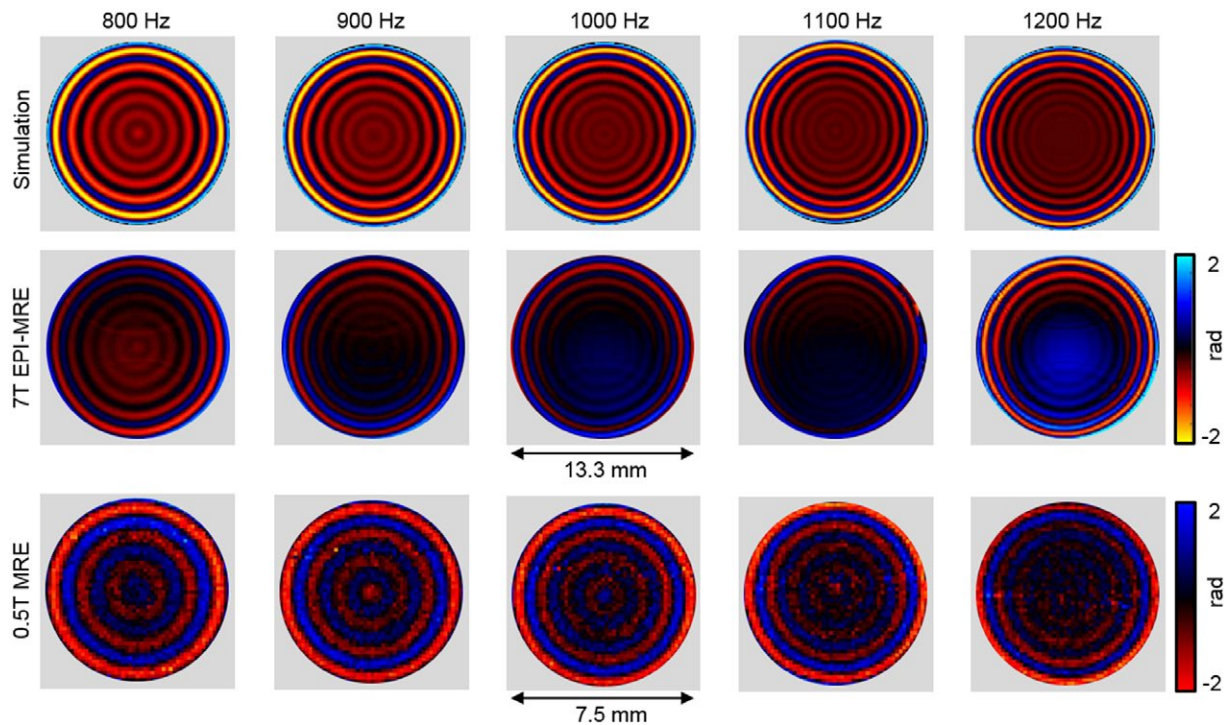


**FIGURE 2** Wave simulations and phantom experiments. Shown are the real parts of the complex-valued wave images that are simulated or acquired in a frequency range of 800–1200 Hz. The 7T EPI MRE sequence was based on the sequence shown in Figure 1B, whereas 0.5T tabletop MRE refers to a compact MRE device with Bessel fit–based shear wave speed calculation for investigations of cylindrical tissue samples<sup>32</sup>

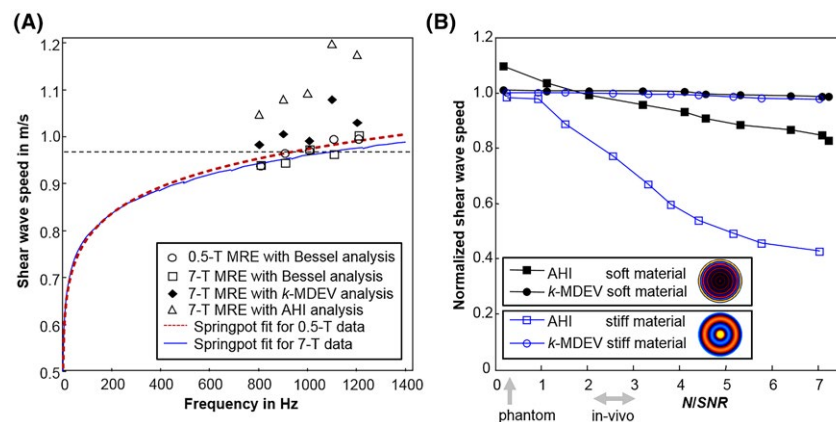


**FIGURE 3** Shear wave speed (SWS) dispersion in phantoms and SNR analysis based on wave simulations. A, Frequency-resolved SWS in the gel phantom calculated by cylindrical wave fitting (Bessel fit), tomoelastography ( $k$ -MDEV), and direct inversion (algebraic Helmholtz inversion [AHI]) of wave images shown in Figure 2. Blue and red curves represent fits of the viscoelastic springpot model on SWS values obtained by Bessel fits of 7T and 0.5T cylindrical wave data. The dashed line represents the reference SWS value of 0.97 m/s used for simulations and obtained from frequency-averaging Bessel-fit analysis of 7T EPI-MRE data. B, Signal-to-noise-ratio analysis for AHI and  $k$ -MDEV using numerical waves. The 2D scalar wave fields in cylindrical coordinates were simulated based on a Bessel function of the first kind to reproduce waves measured in phantoms by tabletop MRE<sup>32</sup> (soft material: SWS = 0.97 m/s as shown in Figure 2; stiff material: SWS = 3.45 m/s as found by in vivo MRE). The ground truth is 1 due to normalization of  $c/c_0$ . Gray arrows demarcate  $N/SNR$  ranges of experiments in the gel phantom and in vivo mouse brain

corresponding frequency-averaged SWS maps are shown in Figure 4E,F. Representative SWS maps of all consecutively acquired slices are found in Supporting Information

Figure S1. Susceptibility-related image distortions are apparent in the MRE magnitude images close to air-filled cavities (e.g., close to the olfactory bulb or the inner ear). Group

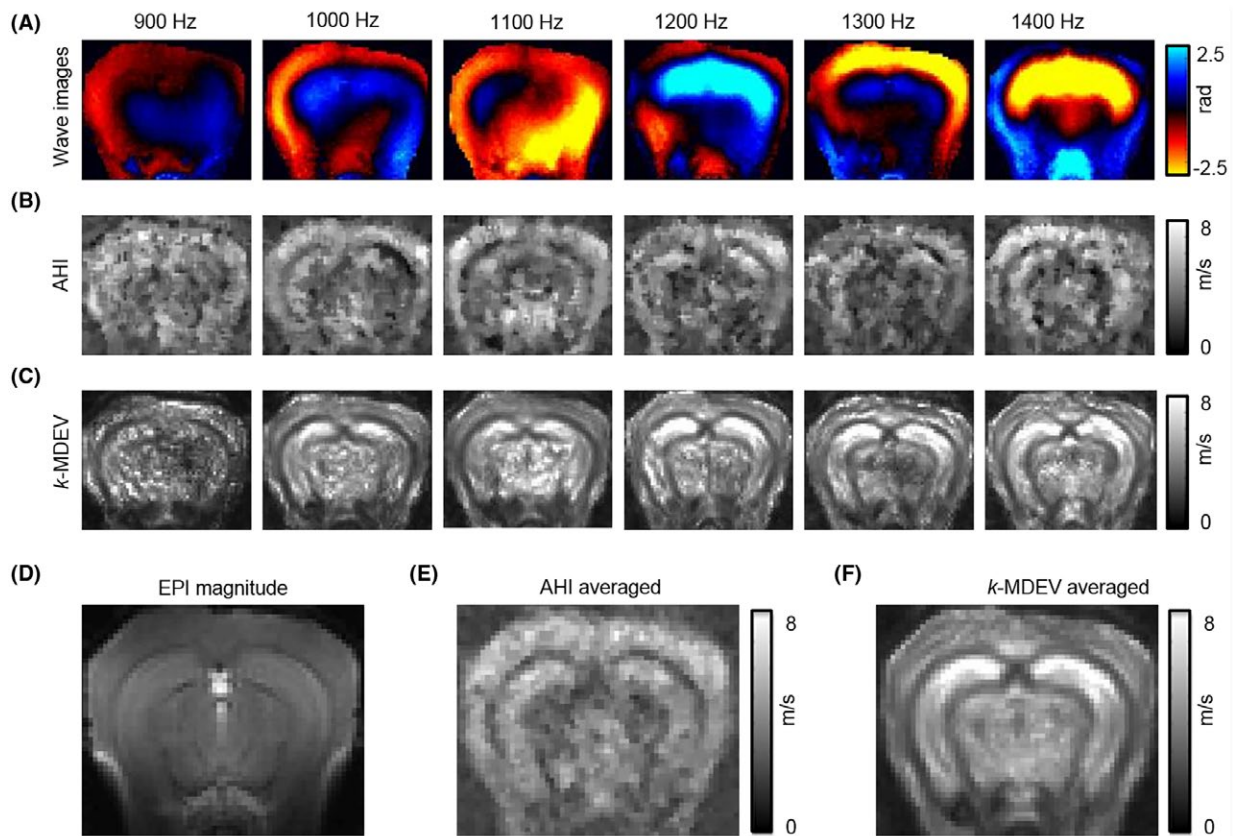


**FIGURE 4** In vivo experiments. A, Frequency-resolved wave images. B, Frequency-resolved SWS maps calculated with AHI. C, Frequency-resolved SWS maps calculated with *k*-MDEV. D, Echo planar magnitude image from the MRE scan. E, Compound, frequency-averaged SWS maps based on AHI. F, Compound, frequency-averaged SWS maps based on *k*-MDEV

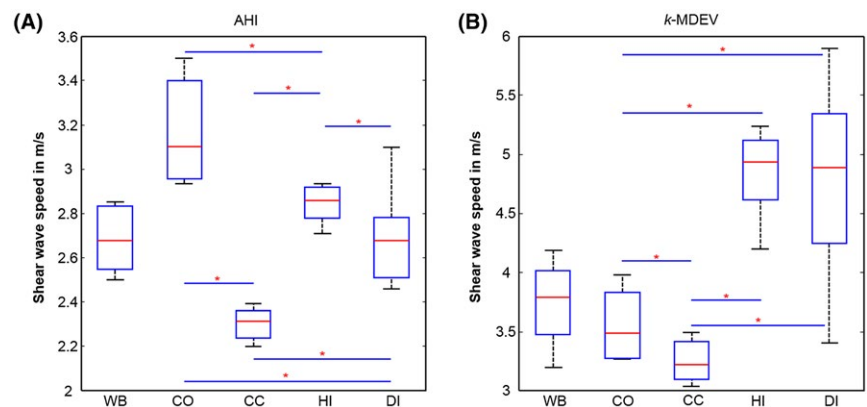


**FIGURE 5** Group values of SWS of in vivo mouse brain based on direct inversion (AHI) and tomoelastography (*k*-MDEV) for whole brain (WB), cerebral cortex (CO), corpus callosum (CC), hippocampus (HI), and diencephalon (DI). \* $P < .05$

mean values were calculated for the whole brain and all segmented subregions visible within the central slice. The results are illustrated in Figure 5 by box plots. The AHI-based SWS analysis (Figure 5A) yielded values of  $2.69 \pm 0.14$  m/s for the whole brain parenchyma (WB), with the highest values in CO ( $3.17 \pm 0.22$  m/s), followed in decreasing order by HI ( $2.87 \pm 0.13$  m/s), DI ( $2.69 \pm 0.19$  m/s), and CC ( $2.30 \pm 0.07$  m/s). The *k*-MDEV SWS analysis (Figure 5B) gave values of  $3.76 \pm 0.33$  m/s for WB, with the highest values for HI ( $4.91 \pm 0.49$  m/s), followed in decreasing

order by DI ( $4.78 \pm 0.78$  m/s), CO ( $3.53 \pm 0.29$  m/s), and CC ( $2.89 \pm 0.17$  m/s). Asterisks in Figure 5 indicate statistically significant differences ( $P < .05$ ) between subregions. All frequency-averaged SWS values are summarized in Table 2. Large variability of SWS values is observed in DI, presumably due to noise and physiological pulsation in that region. Overall, AHI values for the whole-mouse brain are approximately 30% lower than the *k*-MDEV values. The numerical analyses shown in Figure 3B allow us to relate this difference to an undershoot of true values by AHI. Although

**TABLE 2** Shear wave speed values  $\pm$  SDs for the gel phantom and different in vivo brain regions using frequency-averaged AHI and tomoelastography ( $k$ -MDEV)

	SWS (m/s)	
	AHI	$k$ -MDEV
Ultrasound gel	$1.12 \pm 0.19^a$	$1.01 \pm 0.10^a$
Whole brain	$2.69 \pm 0.14$	$3.76 \pm 0.33$
Cortex	$3.17 \pm 0.22$	$3.53 \pm 0.29$
Corpus callosum	$2.30 \pm 0.07$	$2.89 \pm 0.17$
Hippocampus	$2.87 \pm 0.13$	$4.91 \pm 0.49$
Diencephalon	$2.69 \pm 0.19$	$4.78 \pm 0.78$

<sup>a</sup>The SD values in gel samples were derived from the in-plane variation of SWS instead of intragroup SWS as in vivo.

AHI is 15%-30% below ground truth when applied to similar wavelengths as in vivo ( $N$ /SNR between 2 and 3),  $k$ -MDEV has only a 2% offset.

## 4 | DISCUSSION

We introduced fast EPI MRE in the mouse brain. The stability of the method is validated with phantom experiments, SNR analysis, and by comparing in vivo AHI results with previously reported values from the literature.

The ground truth in phantom experiments was determined by Bessel fits of cylindrically emanating waves. This analytical solution of the wave equation in cylindrical coordinates avoids the discretization bias and is not susceptible to noise-related underestimation of SWS values. Therefore, we used 0.5T MRE as reference, as this modality is optimized for generation and analysis of cylindrical waves.<sup>32</sup> This principle, implemented in our 7T MRI scanner, gave similar results, suggesting the stability of the method for measuring ground-truth values and the accuracy of the EPI-MRE sequence.

In our SNR analysis we accounted for 3 types of SNR: displacement, strain and Laplacian, as all 3 have been proposed in the MRE literature as being of particular relevance for judging the validity of values. However, our previous gradient-echo MRE method acquired single-field components only, which does not allow the computation of strain SNR.<sup>22</sup> Comparing our present single-component SNR with SNR of in vivo data,<sup>22</sup> we find similar values of  $8.2 \pm 2.6$  versus  $10.7 \pm 3.3$  for displacement SNR and  $0.80 \pm 0.06$  versus  $0.86 \pm 0.15$  for Laplacian SNR, indicating the consistency of EPI MRE with respect to previously used gradient-echo MRE.

Table 1 gives an overview of the SWS data obtained in the mouse brain using classical direct inversion-based MRE. The in vivo SWS value for the whole brain measured with AHI is in good agreement with the values found in the literature, also indicating the accuracy of the established EPI sequence based on the validation experiments on ultrasound gel. In the present study,  $k$ -MDEV-based SWS is higher

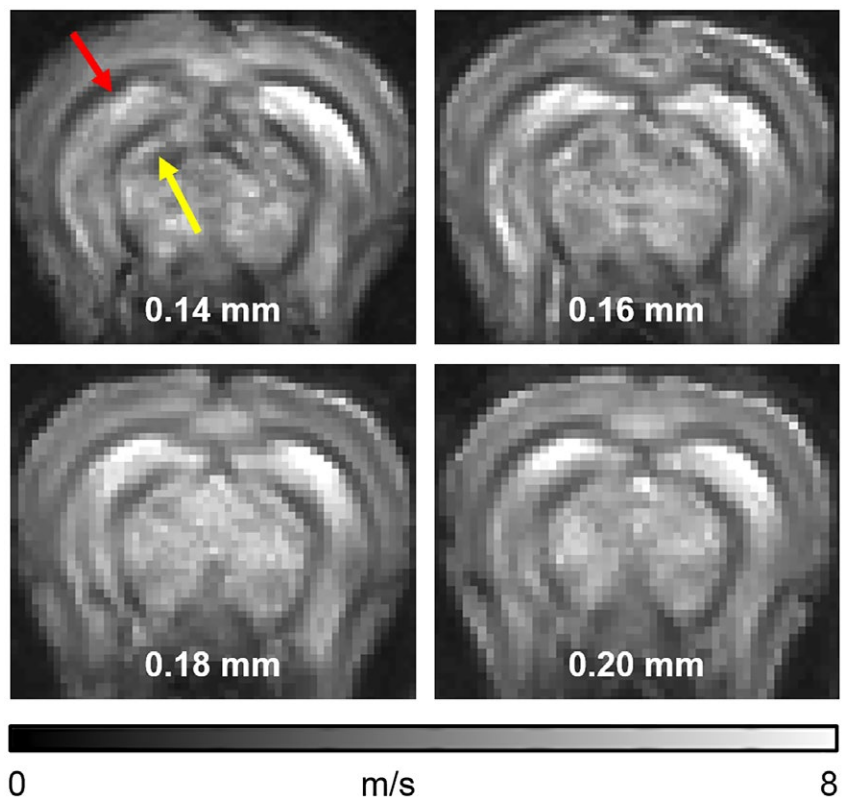


**FIGURE 6** In vivo tomoelastography of the mouse brain with different resolutions. The EPI-MRE-based tomoelastography is shown with resolutions from 0.14 mm to 0.20 mm quadratic pixel edge sizes (pixel size of the present study was 0.18 mm). All resolutions consistently show dark CC tissue (red arrow) and bright hippocampus, indicating the intrinsically softer properties of CC than HI. More detail is visible within the DI at higher resolutions (yellow arrow)

compared with the AHI results. This may be explained by the underestimation of SWS, as demonstrated in Figure 3B. In addition, scan times per single frequency and component are listed in Table 1, indicating that single-shot EPI MRE as used in our study reduces acquisition time by at least a factor of 20. Of note, the overall image quality of EPI MRE is comparable to the data presented in the literature based on gradient-echo MRE.<sup>10,12,23,24</sup> This is an encouraging finding, given the large susceptibility variation in the mouse brain. As shown in Figure 1B,  $T_2^*$  signal dephasing could be reduced by placing the motion-encoding gradients before the refocusing pulse. This strategy reduces TE, as no extra time for motion encoding is needed.

Tomoelastography of the mouse brain supports a more detailed subregional analysis of in vivo stiffness maps compared with classical direct inversion-based MRE. AHI is more strongly biased by noise and discretization artifacts than single-derivative-based  $k$ -MDEV, as shown by simulations and phantom experiments. The observation of lower SDs of AHI in the segmented brain regions than  $k$ -MDEV (Table 2) can be explained in this context by the noise robustness of  $k$ -MDEV probably leading to a more consistent separation of distinct anatomical features, which, however, vary in their stiffness across animals. In general, variability of methods is better represented by in-plane SDs in homogeneous materials such as the phantoms analyzed herein rather than brain values. Tomoelastography better reproduces ground truth from fit-based reconstruction than AHI. In the analyzed SNR range, tomoelastography stays within a 2% error range (Figure 3B).

Regarding regional differences, we found HI to be stiffer than CC in both tomoelastography and AHI. This observation contradicts the published results of invasive ultrasound-based elastography in murine brain.<sup>42</sup> The CC is primarily composed of white matter (WM) fibers, whereas the hippocampus has a large amount of gray matter (GM). Therefore, our findings indicate that GM is stiffer than WM in mouse brain, in contrast to the results of MRE in humans.<sup>6</sup> Invasive atomic force microscopy of cerebellar tissue slices has also shown GM to be stiffer than WM, suggesting that brain stiffness is related to neuronal cell body density.<sup>30</sup> Other studies investigated the contribution of myelin in WM fibers as a mechanical support structure in the brain, suggesting a higher stiffness of WM than GM.<sup>43</sup> In addition, recent dynamic indentation experiments in hippocampal tissues showed that stiffness appears to be lower in areas where cell nuclei density is high.<sup>44</sup> These examples illustrate that regional values of brain stiffness, including WM-GM ratios, provide rich structural information, which still remain to be disentangled. Different dynamic ranges of test methods, prestrains, geometric conditions, and in vivo versus ex vivo conditions including blood perfusion effects translate into different mechanical measures that are hard to compare among different modalities. Additionally,

the type of GM tissue such as deep versus cortical GM has different properties. Recent reports on deep GM in the human brain showed that, for example, the putamen can be stiffer than WM and that its stiffness is correlated with perfusion pressure (MRI-measured perfusion divided by vessel size).<sup>45</sup> Furthermore, anisotropy of macroscopically aligned WM tracks might also contribute to differences in stiffness.<sup>42</sup>

To preliminarily test the appearance of thin structures such as CC in higher-resolution tomoelastography, we performed experiments in a mouse brain by EPI MRE at different resolutions. Figure 6 compares the tomoelastography with pixel edge sizes from 0.2 mm to higher resolution of 0.12 mm. By latter resolution, the spatial support of the thin-layered CC is in the order of 3 to 6 pixels, corresponding to 0.36–0.72 mm, which should be well resolvable by tomoelastography. Consistently, CC appears as dark tissue compared with HI, and more details become visible in DI. Despite the preliminary nature of these experiments, the SWS maps in Figure 6 provide evidence that our CC values reflect intrinsic properties rather than discontinuities due to slip interfaces.<sup>46</sup>

Although we obtained encouraging results, our study has limitations. Figure 6 shows EPI-typical image distortions as further analyzed in Supporting Information Figure S2. The magnitude signal from EPI MRE and from established gradient echo-based MRE used in previous studies<sup>10,12,22,24</sup> were registered to a  $T_2$ -weighted image acquired with standard turbo spin-echo MRI (non-MRE, taken as gold standard). The determinants of the Jacobian deformation matrices provide a measure of the local magnitude deformation,<sup>47</sup> which is 1.0 for no deformation and 0.93 (7% shrinkage) for EPI MRE, in contrast to 1.06 (6% dilation) for gradient-echo MRE considering whole-brain mean values. The similarity of these values indicates a general need for deformation correction in many high-field MRE applications of the mouse. Such correction could be implemented in future studies based on the method proposed by Fehner et al.<sup>48</sup> Furthermore, like all other tomoelastography studies in the literature, the proposed method is 2D.<sup>18</sup> The 2D approach is due to the intrinsic 2D data acquisition in EPI-based MRE. This implies possible overestimation of the wave speed due to out-of-plane shear wave propagation. However, 3D data acquisition is normally achieved by the stacking of 2D images, although the signal between slices is normally jittered, leading to signal variations between adjacent slices<sup>49</sup> and degrading the overall accuracy of elastograms. Values of  $k$ -MDEV and AHI are based on the assumption of local homogeneity, which is better fulfilled in large and macroscopically homogenous abdominal organs than the mouse brain.<sup>20</sup> Nevertheless,  $k$ -MDEV has also been demonstrated to be successful in heterogeneous and smaller tissues such as the kidneys, pancreas, and prostate.<sup>19–21</sup> Heterogeneous inversion methods are being developed and might replace  $k$ -MDEV in future studies of the

mouse brain.<sup>50,51</sup> At any rate, the proposed fast acquisition of multifrequency wave fields will support more sophisticated analysis methods in the future. Another limitation is neglect of the anisotropy of stiffness. Brain tissue is mechanically anisotropic, as demonstrated by Bayly et al. in ex vivo brain samples<sup>52</sup> and by ultrasound elastography<sup>42</sup> or MRE-based waveguide elastography<sup>53</sup> in vivo. Relative differences of values for human brains due to anisotropy are in the range of 33%.<sup>54</sup> For rat brain, 36% have been reported for the specific region of the genu of corpus callosum,<sup>42</sup> whereas 6% were observed for the whole brain. Nevertheless, more elaborate directional filters based on anisotropic shearlets may help to establish tomoelastography as a true 3D inversion method for anisotropic parameter recovery in the future.

## 5 | CONCLUSIONS

In summary, this study introduced multifrequency MRE for tomoelastography of the in vivo mouse brain within short scan times and used this method for analyzing reference SWS values. The relative stiffness difference observed in tomoelastography SWS maps clearly indicated the WM of CC to be softer than cortical or hippocampal tissue. Direct inversion was more severely biased by noise and provided fewer details of mechanical parameters than tomoelastography. The new method contributes to the growing understanding of mechanical signatures of brain tissues and is potentially of great value for future studies of in vivo brain mechanical properties in health and disease.

## ORCID

Eric Barnhill  <http://orcid.org/0000-0002-1832-7197>

Jürgen Braun  <http://orcid.org/0000-0001-5183-7546>

## REFERENCES

1. Moeendarbary E, Weber IP, Sheridan GK, et al. The soft mechanical signature of glial scars in the central nervous system. *Nat Commun*. 2017;8:14787.
2. Hirsch S, Braun J, Sack I. *Magnetic Resonance Elastography—Physical Background and Medical Applications*. Weinheim, Germany: Wiley-VCH; 2017.
3. Chatelin S, Constantinesco A, Willinger R. Fifty years of brain tissue mechanical testing: from in vitro to in vivo investigations. *Biorheology*. 2010;47:255–276.
4. Hiscox LV, Johnson CL, Barnhill E, et al. Magnetic resonance elastography (MRE) of the human brain: technique, findings and clinical applications. *Phys Med Biol*. 2016;61:R401–R437.
5. Arani A, Murphy MC, Glaser KJ, et al. Measuring the effects of aging and sex on regional brain stiffness with MR elastography in healthy older adults. *NeuroImage*. 2015;111:59–64.
6. Braun J, Guo J, Lutzkendorf R, et al. High-resolution mechanical imaging of the human brain by three-dimensional multifrequency magnetic resonance elastography at 7T. *NeuroImage*. 2014;90:308–314.
7. Dittmann F, Hirsch S, Tzschatzsch H, Guo J, Braun J, Sack I. In vivo wideband multifrequency MR elastography of the human brain and liver. *Magn Reson Med*. 2016;76:1116–1126.
8. Johnson CL, Holtrop JL, McGarry MD, et al. 3D multislabs, multishot acquisition for fast, whole-brain MR elastography with high signal-to-noise efficiency. *Magn Reson Med*. 2014;71:477–485.
9. Atay SM, Kroenke CD, Sabet A, Bayly PV. Measurement of the dynamic shear modulus of mouse brain tissue in vivo by magnetic resonance elastography. *J Biomech Eng*. 2008;130:021013.
10. Klein C, Hain EG, Braun J, et al. Enhanced adult neurogenesis increases brain stiffness: in vivo magnetic resonance elastography in a mouse model of dopamine depletion. *PLoS ONE*. 2014;9:e92582.
11. Murphy MC, Curran GL, Glaser KJ, et al. Magnetic resonance elastography of the brain in a mouse model of Alzheimer's disease: initial results. *Magn Reson Imaging*. 2012;30:535–539.
12. Riek K, Millward JM, Hamann I, et al. Magnetic resonance elastography reveals altered brain viscoelasticity in experimental autoimmune encephalomyelitis. *Neuroimage Clin*. 2012;1:81–90.
13. Honarvar M, Sahebjavaher R, Sinkus R, Rohling R, Salcudean SE. Curl-based finite element reconstruction of the shear modulus without assuming local homogeneity: time harmonic case. *IEEE Trans Med Imaging*. 2013;32:2189–2199.
14. McGarry MD, Van Houten EE, Johnson CL, et al. Multiresolution MR elastography using nonlinear inversion. *Med Phys*. 2012;39:6388–6396.
15. Oliphant TE, Manduca A, Ehman RL, Greenleaf JF. Complex-valued stiffness reconstruction for magnetic resonance elastography by algebraic inversion of the differential equation. *Magn Reson Med*. 2001;45:299–310.
16. Papazoglou S, Hamhaber U, Braun J, Sack I. Algebraic Helmholtz inversion in planar magnetic resonance elastography. *Phys Med Biol*. 2008;53:3147–3158.
17. Manduca A, Lake DS, Kruse SA, Ehman RL. Spatio-temporal directional filtering for improved inversion of MR elastography images. *Med Image Anal*. 2003;7:465–473.
18. Tzschatzsch H, Guo J, Dittmann F, et al. Tomoelastography by multifrequency wave number recovery from time-harmonic propagating shear waves. *Med Image Anal*. 2016;30:1–10.
19. Dittmann F, Reiter R, Guo J, et al. Tomoelastography of the prostate using multifrequency MR elastography and externally placed pressurized-air drivers. *Magn Reson Med*. 2018;79:1325–1333.
20. Dittmann F, Tzschatzsch H, Hirsch S, et al. Tomoelastography of the abdomen: tissue mechanical properties of the liver, spleen, kidney, and pancreas from single MR elastography scans at different hydration states. *Magn Reson Med*. 2017;78:976–983.
21. Marticorena Garcia SR, Grossmann M, Lang ST, et al. Tomoelastography of the native kidney: regional variation and physiological effects on in vivo renal stiffness. *Magn Reson Med*. 2018;79:2126–2134.
22. Munder T, Pfeffer A, Schreyer S, et al. MR elastography detection of early viscoelastic response of the murine hippocampus to amyloid beta accumulation and neuronal cell loss due to Alzheimer's disease. *J Magn Reson Imaging*. 2018;47:105–114.

23. Hain EG, Klein C, Munder T, et al. Dopaminergic neurodegeneration in the mouse is associated with decrease of viscoelasticity of substantia nigra tissue. *PLoS ONE*. 2016;11:e0161179.
24. Millward JM, Guo J, Berndt D, Braun J, Sack I, Infante-Duarte C. Tissue structure and inflammatory processes shape viscoelastic properties of the mouse brain. *NMR Biomed*. 2015;28:831–839.
25. Schregel K, Wuerfel E, Garteiser P, et al. Demyelination reduces brain parenchymal stiffness quantified in vivo by magnetic resonance elastography. *Proc Natl Acad Sci USA*. 2012;109:6650–6655.
26. Freimann FB, Muller S, Streitberger KJ, et al. MR elastography in a murine stroke model reveals correlation of macroscopic viscoelastic properties of the brain with neuronal density. *NMR Biomed*. 2013;26:1534–1539.
27. Pong AC, Jugé L, Bilston LE, Cheng S. Development of acute hydrocephalus does not change brain tissue mechanical properties in adult rats, but in juvenile rats. *PLoS ONE*. 2017;12:e0182808.
28. Li J, Jamin Y, Boulton JK, et al. Tumour biomechanical response to the vascular disrupting agent ZD6126 in vivo assessed by magnetic resonance elastography. *Br J Cancer*. 2014;110:1727–1732.
29. Patz S, Nazari N, Barbone PE, et al. Functional neuroimaging in the brain using magnetic resonance elastography. In: Proceedings of the 25th Annual Meeting of ISMRM, Honolulu, HI; 2017: 242.
30. Christ AF, Franze K, Gautier H, et al. Mechanical difference between white and gray matter in the rat cerebellum measured by scanning force microscopy. *J Biomech*. 2010;43:2986–2992.
31. Manduca A. MR elastography: standardizing terminology and setting guidelines. In: Proceedings of the 1st International MRE Workshop, Berlin, Germany; 2017: 12.
32. Braun J, Tzschatzsch H, Korting C, et al. A compact 0.5 T MR elastography device and its application for studying viscoelasticity changes in biological tissues during progressive formalin fixation. *Magn Reson Med*. 2018;79:470–478.
33. Okamoto RJ, Clayton EH, Bayly PV. Viscoelastic properties of soft gels: comparison of magnetic resonance elastography and dynamic shear testing in the shear wave regime. *Phys Med Biol*. 2011;56:6379–6400.
34. Yasar TK, Royston TJ, Magin RL. Wideband MR elastography for viscoelasticity model identification. *Magn Reson Med*. 2013;70:479–489.
35. Ipek-Ugay S, Driessle T, Ledwig M, et al. Tabletop magnetic resonance elastography for the measurement of viscoelastic parameters of small tissue samples. *J Magn Reson*. 2015;251:13–18.
36. Donoho DL, Johnstone IM, Kerkycharian G, Picard D. Wavelet shrinkage—asymptopia. *J Roy Stat Soc B Met*. 1995;57:301–337.
37. Barnhill E, Hollis L, Sack I, et al. Nonlinear multiscale regularisation in MR elastography: towards fine feature mapping. *Med Image Anal*. 2017;35:133–145.
38. Selesnick IW, Baraniuk RG, Kingsbury NG. The dual-tree complex wavelet transform. *IEEE Signal Process Mag*. 2005;22:123–151.
39. McGarry MD, Van Houten EE, Perrinez PR, Pattison AJ, Weaver JB, Paulsen KD. An octahedral shear strain-based measure of SNR for 3D MR elastography. *Phys Med Biol*. 2011;56:N153–N164.
40. Manduca A, Lake DS, Huynh KT, Eon RS, Annoni EM, Ehman RL. Consistent SNR measures for magnetic resonance elastography. In: Proceedings of the 23rd Annual Meeting of ISMRM, Toronto, Canada; 2015: 2519.
41. Arunachalam SP, Rossman PJ, Arani A, et al. Quantitative 3D magnetic resonance elastography: comparison with dynamic mechanical analysis. *Magn Reson Med*. 2017;77:1184–1192.
42. Mace E, Cohen I, Montaldo G, Miles R, Fink M, Tanter M. In vivo mapping of brain elasticity in small animals using shear wave imaging. *IEEE Trans Med Imaging*. 2011;30:550–558.
43. Budday S, Nay R, de Rooij R, et al. Mechanical properties of gray and white matter brain tissue by indentation. *J Mech Behav Biomed Mater*. 2015;46:318–330.
44. Antonovaitis N, Beekmans SV, Hol EM, Wadman WJ, Iannuzzi D. Structure-stiffness relation of live mouse brain tissue determined by depth-controlled indentation mapping. arXiv 2018;1802.02245v1.
45. Hetzer S, Birr P, Fehlner A, et al. Perfusion alters stiffness of deep gray matter. *J Cereb Blood Flow Metab*. 2018;38:116–125.
46. Yin Z, Glaser KJ, Manduca A, et al. Slip interface imaging predicts tumor-brain adhesion in vestibular schwannomas. *Radiology*. 2015;277:507–517.
47. von Holst H, Li X, Kleiven S. Increased strain levels and water content in brain tissue after decompressive craniotomy. *Acta Neurochir*. 2012;154:1583–1593.
48. Fehlner A, Hirsch S, Weygandt M, et al. Increasing the spatial resolution and sensitivity of magnetic resonance elastography by correcting for subject motion and susceptibility-induced image distortions. *J Magn Reson Imaging*. 2017;46:134–141.
49. Hirsch S, Klatt D, Freimann F, Scheel M, Braun J, Sack I. In vivo measurement of volumetric strain in the human brain induced by arterial pulsation and harmonic waves. *Magn Reson Med*. 2013;70:671–683.
50. Barnhill E, Davies PJ, Ariyurek C, Fehlner A, Braun J, Sack I. Heterogeneous multifrequency direct inversion (HMDFI) for magnetic resonance elastography with application to a clinical brain exam. *Med Image Anal*. 2018;46:180–188.
51. Honarvar M, Sahebjavaher RS, Rohling R, Salcudean SE. A comparison of finite element-based inversion algorithms, local frequency estimation, and direct inversion approach used in MRE. *IEEE Trans Med Imaging*. 2017;36:1686–1698.
52. Feng Y, Okamoto RJ, Namani R, Genin GM, Bayly PV. Measurements of mechanical anisotropy in brain tissue and implications for transversely isotropic material models of white matter. *J Mech Behav Biomed Mater*. 2013;23:117–132.
53. Romano A, Guo J, Prokscha T, et al. In vivo waveguide elastography: effects of neurodegeneration in patients with amyotrophic lateral sclerosis. *Magn Reson Med*. 2014;72:1755–1761.
54. Anderson AT, Van Houten E, McGarry M, et al. Observation of direction-dependent mechanical properties in the human brain with multi-excitation MR elastography. *J Mech Behav Biomed Mater*. 2016;59:538–546.
55. Clayton EH, Garbow JR, Bayly PV. Frequency-dependent viscoelastic parameters of mouse brain tissue estimated by MR elastography. *Phys Med Biol*. 2011;56:2391–2406.
56. Jamin Y, Boulton J, Li J, et al. Exploring the biomechanical properties of brain malignancies and their pathologic determinants in vivo with magnetic resonance elastography. *Cancer Res*. 2015;75:1216–1224.
57. Boulet T, Kelso ML, Othman SF. Long-term in vivo imaging of viscoelastic properties of the mouse brain after controlled cortical impact. *J Neurotrauma*. 2013;30:1512–1520.

## SUPPORTING INFORMATION

Additional supporting information may be found online in the Supporting Information section at the end of the article.

**FIGURE S1** Mouse brain coverage by 5 consecutive axial slices measured by the developed single-shot spin-echo EPI-MRE sequence. Upper row shows the magnitude of the MRE signal (susceptibility-related distortions at the inferior parts of the cerebral cortex are indicated by red arrows); and bottom row shows the SWS maps from tomoelastography

**FIGURE S2** Analysis of image distortions resulted by new single-shot EPI MRE and conventional gradient-echo (GRE) MRE as used in previous work.<sup>10,12,22,24</sup> Image distortions due to long TE are visible in the magnitude images of both EPI MRE and GRE MRE compared with a  $T_2$ -weighted image acquired with standard turbo spin-echo (TSE) MRI (the red

encircled region refers to reference anatomy). As demonstrated in Supporting Information Figure S1, the most severe artifacts arise at the inferior parts of the cerebral cortex. The amount of deformation necessary to register EPI-MRE and GRE-MRE images to the reference TSE image can be quantified by the determinant of the Jacobian.<sup>47</sup> Based on these Jacobian determinants, similar magnitudes of deformations were found for the entire brain (0.93, 7% shrinkage for EPI MRE; 1.06, 6% dilation for GRE MRE). References are contained in the main document

**How to cite this article:** Bertalan G, Guo J, Tzschätzsch H, et al. Fast tomoelastography of the mouse brain by multifrequency single-shot MR elastography. *Magn Reson Med*. 2019;81:2676–2687. <https://doi.org/10.1002/mrm.27586>